Article

Probing the critical nucleus size for ice formation with graphene oxide nanosheets

Guoying Bai[1,2], Dong Gao[3], Zhang Liu[1], Xin Zhou[4,5,6]* & Jianjun Wang[1,6,7]*

Water freezing is ubiquitous and affects areas as diverse as climate, the chemical industry, cryobiology and materials science. Ice nucleation is the controlling step in water freezing[1–5] and has, for nearly a century, been assumed to require the formation of a critical ice nucleus[6–10]. But there has been no direct experimental evidence for the existence of such a nucleus, owing to its transient and nanoscale nature[6,7]. Here we report ice nucleation in water droplets containing graphene oxide nanosheets of controlled sizes and show that they have a notable impact on ice nucleation only above a certain size that varies with the degree of supercooling of the droplets. We infer from our experimental data and theoretical calculations that the critical size of the graphene oxide reflects the size of the critical ice nucleus, which in the case of sufficiently large graphene oxides sits on their surface and gives rise to ice formation behaviour consistent with classical nucleation theory. By contrast, when the graphene oxide size is smaller than that of the critical ice nucleus, pinning at the periphery of the graphene oxide deforms the ice nucleus as it grows. This gives rise to a much higher free-energy barrier for nucleation and suppresses the promoting effect of the graphene oxide[11]. The results provide experimental information on the existence and temperature-dependent size of the critical ice nucleus, which has previously only been explored theoretically and through simulations[12–16]. As pinning of a pre-critical nucleus at a nanoparticle edge is not specific to the ice nucleus on graphene oxides, we expect that our approach could be extended to probe the critical nuclei in other nucleation processes.

Theory[17] and experiment[18] have shown that for radii ranging from around 10 Å to 1,000 Å, size profoundly influences a particle's ability to induce ice nucleation. Such a size effect is evident when we consider that antifreeze proteins (AFPs) suppress ice formation, whereas structurally similar but larger ice nucleation proteins (INPs) promote it (Fig. 1a, b)[19–21]. Because graphene oxide (GO) nanosheets influence ice nucleation[22–25] and can be prepared in a wide range of sizes, we used them to systematically explore the effect of nanoparticle size on ice nucleation.

GOs with different sizes were prepared by fractionating commercial GO aqueous dispersions by consecutively filtering through ultrafiltration membranes (Ultracel) with different molecular weight cut-offs (see Methods). Figure 1d–h shows transmission electron microscopy (TEM) images of GO fractions with average lateral sizes of 3 nm, 8 nm, 11 nm, 21 nm and 50 nm, respectively, along with the size distribution of each fraction. Atomic force microscopy (AFM) imaging indicates that the GOs have roughly the same thickness, irrespective of size (Extended Data Fig. 1a). Detailed characterizations of GOs with dynamic light scattering, X-ray photoelectron spectroscopy, Raman spectroscopy and nuclear magnetic resonance spectroscopy (see Extended Data Table 1

and Supplementary Figs. 1–5 for details) and cryo-TEM (Extended Data Fig. 1b) further consolidate that readily water-dispersible thin plate-like GOs with various sizes were obtained.

Ice nucleation activities were then probed by using optical microscopy to determine mean ice nucleation temperatures (T_{IN}) of water droplets containing GOs of different sizes (Methods). The top and bottom row images in Fig. 2a illustrate typical freezing behaviours seen in water droplets containing GOs with an average lateral size of 8 nm and 11 nm, respectively. Strikingly, the T_{IN} of the droplet containing 8-nm GOs is −27.6 °C (Supplementary Video 1), which is about 10 °C lower than that of a droplet containing 11-nm GOs under otherwise identical experimental conditions (Supplementary Video 2).

Figure 2b summarizes the results of our systematic exploration. We find that below 8 nm, T_{IN} is about −27.5 °C and independent of GO size and concentration, and that it is equal to the T_{IN} measured under identical conditions for water droplets without added GOs. Because the homogeneous T_{IN} is lower than the T_{IN} that we see in this regime[26,27], we infer that ice formation is triggered by interfaces other than those of GO, for example the water–substrate interface (Extended Data Fig. 2b). When moving from GOs with a size of 8 nm to GOs with a size of 11 nm,

[1]Key Laboratory for Green Printing, Beijing National Laboratory for Molecular Science, Institute of Chemistry, Chinese Academy of Sciences, Beijing, China. [2]Research Institute for Energy Equipment Materials, School of Materials Science and Engineering, Hebei University of Technology, Tianjin, China. [3]Key Laboratory of Hebei Province for Molecular Biophysics Institute of Biophysics, Hebei University of Technology, Tianjin, China. [4]School of Physical Sciences and CAS Center for Excellence in Topological Quantum Computation, University of Chinese Academy of Sciences, Beijing, China. [5]Wenzhou Institute, University of Chinese Academy of Sciences, Wenzhou, China. [6]Songshan Lake Materials Laboratory, Dongguan, Guangdong, China. [7]School of Future Technology, University of Chinese Academy of Sciences, Beijing, China. *e-mail: xzhou@ucas.ac.cn; wangj220@iccas.ac.cn
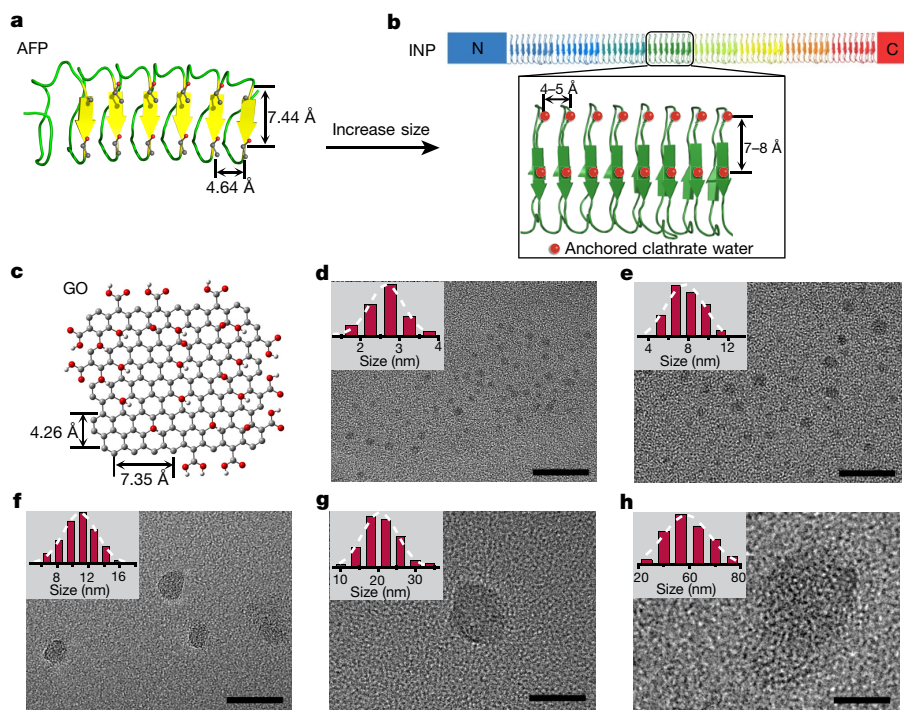
Fig. 1 | GOs of controlled sizes. a, Ribbon illustration of the antifreeze protein developed by the mealworm *Tenebrio molitor* (*Tm*AFP). **b,** Schematic representation of monomer of ice nucleation protein in the bacterium *Pseudomonas syringae* (*Ps*INP). The central tandem repeats of *Ps*INPs have almost the same β-solenoid structure as that of *Tm*AFP. Both proteins share a similar lattice feature with that of ice crystals[19,20]. The main difference is that the central β-solenoid region of *Ps*INPs is almost ten times as large as that of *Tm*AFP. **c,** Illustration of GO nanosheets. Carbon, grey; oxygen, red; hydrogen, white. **d–h,** TEM images of various-sized GOs (see Methods). All the scale bars are 20 nm. The insets in **d–h** are the corresponding size distributions of the GOs. Each size distribution is obtained by analysing the lateral diameters of more than 100 GOs imaged by TEM.
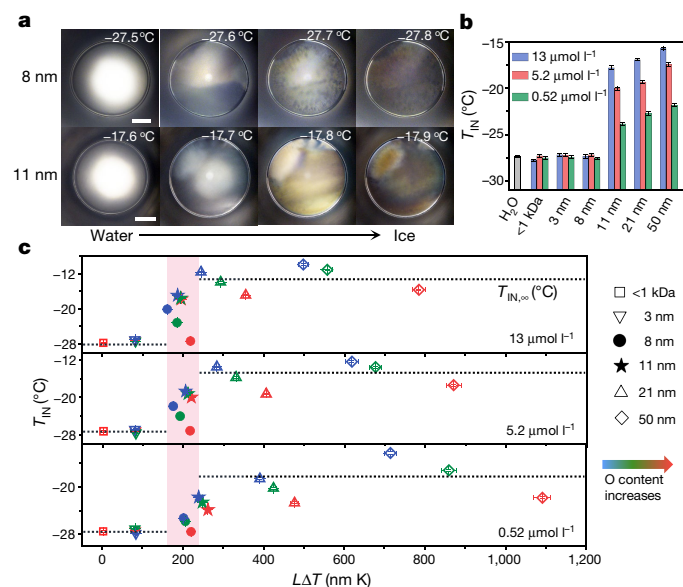

Fig. 2 | Ice nucleation activities of GOs with different sizes and oxidation degrees. a, Optical microscopic images showing typical freezing processes of water droplets (0.2 μl) containing GOs with average lateral sizes of 8 nm (upper row) and 11 nm (lower row) when the temperature was lowered at a cooling rate of 5 °C min^{-1}. The GO concentrations in the water droplets are the same (13 μmol l^{-1}). Scale bar, 200 μm. **b,** T_{IN} of water droplets (0.2 μl) containing GOs of controlled sizes, at three different concentrations. Cooling rate, 5 °C min^{-1}. Data are the mean ± the standard error on the mean (s.e.m.). For each mean, the total number of measurements is about 150. **c,** The relationship between T_{IN} and $L\Delta T$ (the supercooling scaled size of GOs, $\Delta T = T_m - T_{IN}$) for three different concentrations of GOs with six sizes and three oxidation extents. Data are means. The error bars for T_{IN} are s.e.m., and the error bars for $L\Delta T$ are calculated according to the s.e.m. of L and T_{IN} based on the error propagation formulae. For each mean of T_{IN} or L, the total number of measurements is about 150.

we see an abrupt increase of about 10 °C in T_{IN}. The abrupt change persists when using different GO concentrations (Fig. 2b, and Extended Data Fig. 3), GOs with different degrees of oxidation (see Extended Data Table 2 and Supplementary Figs. 6–12 for details) and different cooling rates (Extended Data Fig. 4). Above 11 nm, further increases in GO size give rise to only slight further increases in T_{IN}.

The abrupt change in T_{IN} occurs at $L\Delta T \approx 200$ nm K (Fig. 2c); here L is the average lateral size of GOs, and $\Delta T = T_m - T_{IN}$, with T_m being the equilibrium melting temperature of ice. When $L\Delta T < 200$ nm K, ice nucleation occurs on the water–substrate interface and is little influenced by the presence of GOs. When $L\Delta T > 200$ nm K, T_{IN} is almost independent of the value of $L\Delta T$ but varies with GO concentration and corresponds to the normal heterogeneous ice nucleation temperature $T_{IN,\infty}(C)$ associated with GOs large enough to induce ice nucleation. Note that we neglect the small changes in nucleation temperature associated with changes in the oxygen content of the investigated GOs.

The ice nucleation activity of GO sheets itself thus exhibits a transition when $L\Delta T \approx 200$ nm K, which for GOs of any specific size L should occur at the supercooling temperature $\Delta T_L \approx (200 \text{ nm}/L)$ K. As the degree of supercooling reached before heterogeneous ice nucleation sets in depends on the number, n, of contained GO sheets, we verify the expected change in GO ice nucleation activity by measuring T_{IN} for water droplets containing GOs from the same size fraction but in different numbers n (achieved by varying the concentration, the droplet volume or both). This largely excludes features unique to the differently sized GOs from influencing the ice nucleation trends that we see. As shown in Fig. 3a, we find for GOs with $L = 8$ nm, 11 nm and 21 nm respectively that T_{IN} increases with the logarithm of n only when $\Delta T > \Delta T_L$, revealing that at this temperature range, GO is active in facilitating ice nucleation; GO does not show an obvious effect on ice nucleation after $\Delta T \leq \Delta T_L$, as indicated by the fact that T_{IN} remains almost constant as the logarithm of n increases. The same behaviour is seen for GOs with three different oxygen contents (all with $L = 11$ nm) (Extended Data Fig. 5a).

We also measured ice nucleation delay times (t_D) as a function of supercooling (Fig. 3b), again finding a distinct change in t_D at the expected size-dependent supercooling $\Delta T_L \approx (200 \text{ nm}/L)$ K. This was seen with the 8-nm, 11-nm and 21-nm GO samples, which were each used
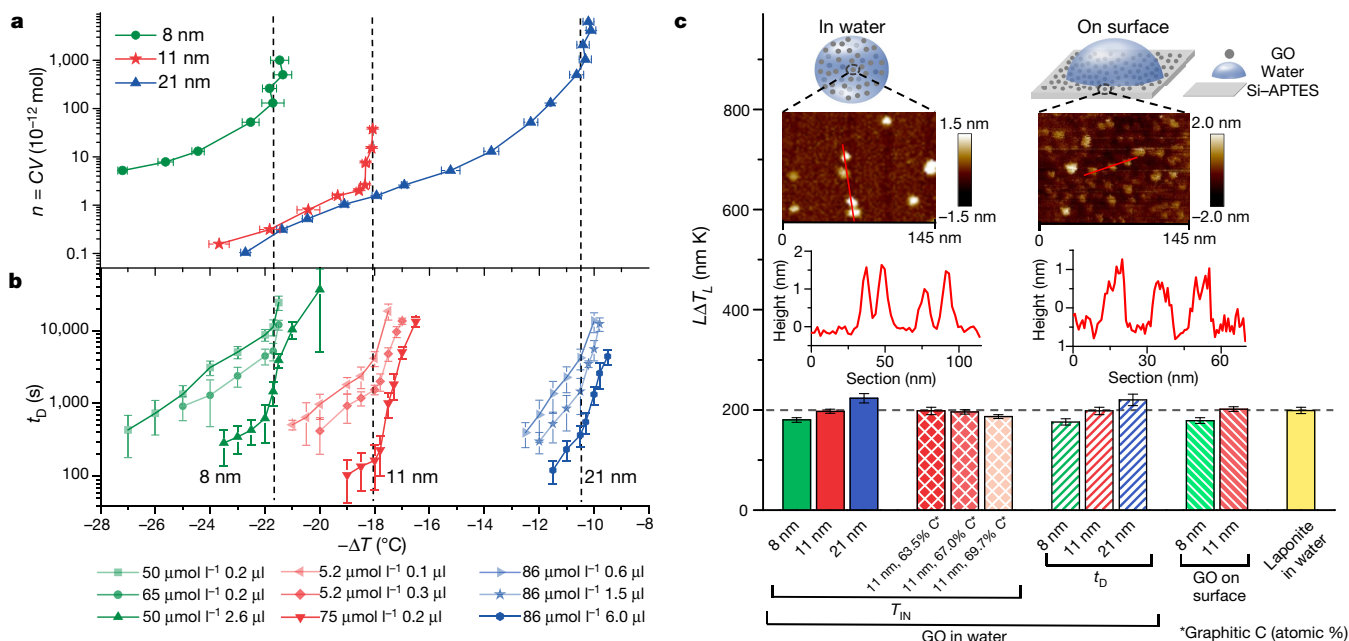
Fig. 3 | Transitions in the ice nucleation activity of nanosheets. a, The supercooling temperature of ice nucleation versus number of GOs in water droplet, $n = CV$, where C is the concentration of the GO aqueous dispersion and V is the volume of an individual droplet (data in Supplementary Table 1). Data are means ±s.e.m. For each mean, the total number of measurements is about 50. **b**, The ice nucleation delay time for water droplets versus the supercooling ΔT. Data are means; error bars are standard deviation estimated by the jackknife resampling technique. For each mean, the total number of measurements varies from 20 to 150 to ensure that the nucleation event number m is typically not less than 10 (see Methods). **c**, The obtained $L\Delta T_L$ for anisotropic nanosheets. Here ΔT_L is the supercooling temperature at which the transition happens. Insets show schematic diagrams of water droplets containing GO nanosheets or water droplets deposited on the substrate anchored with GO nanosheets as well as the corresponding AFM images of GOs (see Methods), together with heights through the cross-section (obtained by AFM). Data are means; error bars of $L\Delta T_L$ are calculated according to the s.e.m. of ΔT_L or L based on the error propagation formulae. For each mean of T_{IN} and L, the total number of measurements is about 50 and 100, respectively. Here the cooling rate is always 5 °C min^{-1}.

with three different values of n, giving $\tau(T) = n t_D(T; n)$. The obtained $\tau(T)$ is independent of the number of GOs in aqueous dispersion within experimental error (Extended Data Fig. 5b), which agrees with the theoretical analysis (see Methods).

Figure 3c summarizes our experimental findings, illustrating that all investigated nanosheets exhibit an abrupt change in their ability to facilitate ice nucleation at ΔT_L, with a small deviation of only about 10%. This holds for ΔT_L inferred from different measurements (T_{IN} and t_D), different kinds of materials (GOs and laponite nanosheets, Extended Data Fig. 6) and different exposure of the nanosheets (either dispersed in water or anchored on a substrate, Extended Data Fig. 7). Note that measurements on the GO nanosheets anchored on solid surfaces exclude the possible influence on ice nucleation due to diffusion of GOs and the interplay among GO nanosheets when dispersed in water.

We can infer the free-energy barrier of ice nucleation (ΔG^*) from both $n(T)$ and $\tau(T)$ (see Methods), with Fig. 4a showing that the values collapse into the same line, that is, $\Delta G^* \propto \Delta T^{-2}$, over a small temperature range when $\Delta T > \Delta T_L$, consistent with classical nucleation theory (CNT). Importantly, ΔG^* shows an abrupt change at ΔT_L in all cases, revealing that the source of the abrupt change in ice nucleation activity of GOs is the change in the free-energy barrier for ice nucleation. The dependence of the free-energy barrier on the size of nanosheets is known to be based on the dimensionless variable, $l = L/(2R_c)$, that is, the relative size of the nanosheets to the radius R_c of the critical ice nucleus. Therefore, the transition of ΔG^* found experimentally to occur at the specific value of the dimensionless size of GO, $L_c/(2R_c) = l_c$, corresponds to $L_c\Delta T \approx 200$ nm K; as such, we have $R_c = (100 \text{ nm K})/(l_c\Delta T) \propto \Delta T^{-1}$, consistent with CNT.

We explore this further by using CNT to calculate the free-energy barrier of ice nucleation on finite-sized GO nanosheets, consolidating that ΔG^* is a function of the dimensionless size of nanosheets and

has a transition at $l_c \approx 1$ almost regardless of the detailed features of nanosheets such as the shape and the interaction with ice (Fig. 4b; see Methods for more details). As sketched in Fig. 4c (and Extended Data Fig. 8), when $L \approx 2R_c$, two critical ice nuclei need to form in succession, and two corresponding free-energy barriers must be overcome. When $l > l_c$, the first free-energy barrier is the major one: the corresponding critical ice nucleus is a spherical cap with a small contact angle sitting on the surface of GO, the same as the heterogeneous ice nucleation atop GOs of sufficiently large size. By contrast, when $l < l_c$, the growing ice nucleus changes its shape after meeting the edge of GO and leads the second free-energy barrier to be the greater one. The corresponding critical ice nucleus is a spherical cap with a large contact angle due to the pinning at the edge of GO. Here the pinning is not due to any specific interaction of the edge of the GO with the water or ice, but is the requirement for minimizing the total interfacial free energy of the ice nucleus (see Methods); thus it is general. Therefore, the transition occurs when the major free-energy barrier alters from one to the other as l varies across the l_c at which the two free-energy barriers are equal.

Since $L_c/(2R_c) = l_c \approx 1$ from the theoretical calculation, we conclude that the critical size of GO, L_c, is approximately equal to the diameter of the critical ice nucleus, thus $R_c \approx (100/\Delta T)$ nm (where ΔT is in kelvin). According to CNT, $R_c = 2\gamma/|\Delta\mu|$, and we can obtain the interfacial energy between ice and water to be $\gamma \approx 45$ mJ m^{-2}, if using a typical value of the chemical potential difference between ice and water, $\Delta\mu \approx -893\Delta T$ mJ cm^{-3}. Note that the value of γ cannot be directly measured experimentally, and the reported γ has a large range from 23 mJ m^{-2} to 54 mJ m^{-2} in the literature[13,28,29]. The current method provides a way to measure the value of γ. Our results also show that surfaces with a pattern size comparable to that of the critical ice nucleus (for example,
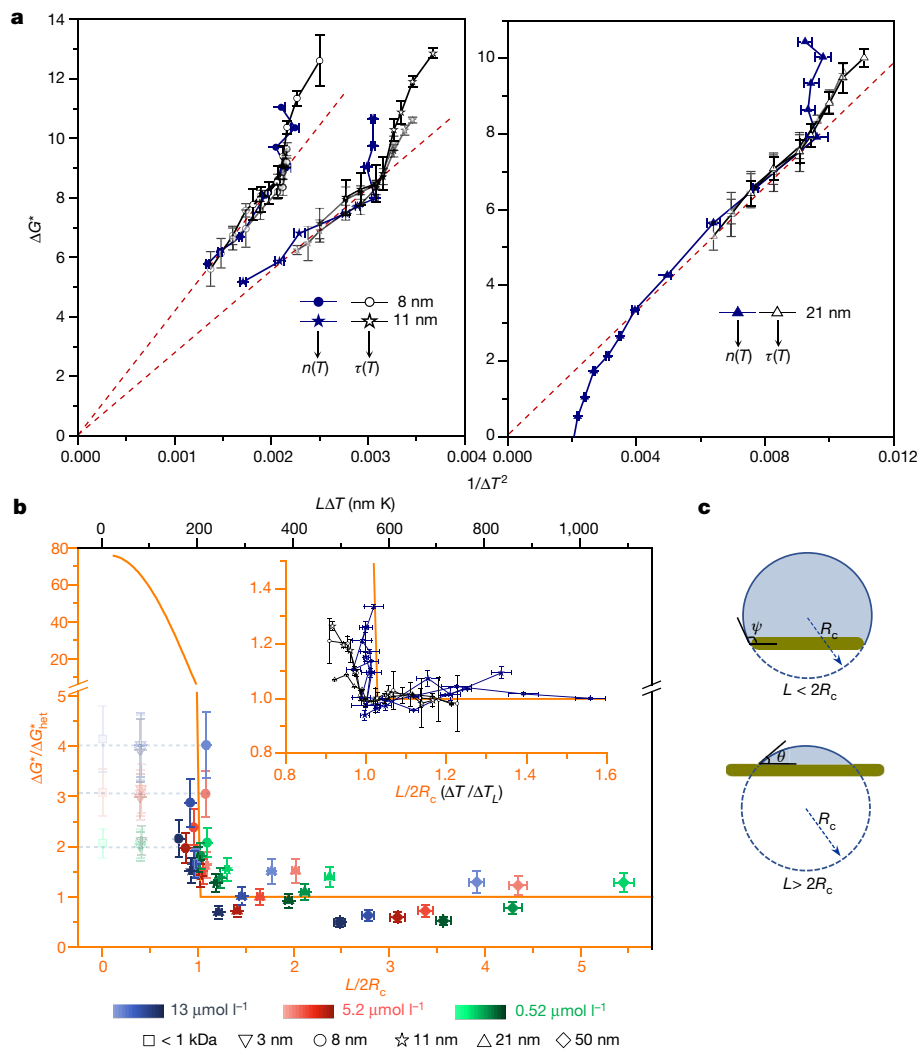
Fig. 4 | Abrupt change in the free-energy barrier of ice nucleation on GO nanosheets. a, The free-energy barrier ΔG^* (with units of $k_B T$) is obtained from the curves of $n(T)$ and $\tau(T)$, respectively (see Methods). The T_{IN} data for $n(T)$ here are medians ± the standard error of the median (estimated as 1.2533 s.e.m.). For each median, the total number of measurements is about 50. The data for $\tau(T)$ are from Fig. 3b, including the data for all three different numbers of GOs (indicated by three different transparencies). The dashed line gives ΔG^*_{het}, the free-energy barrier of the normal heterogeneous nucleation on sufficiently large GOs. **b**, The free-energy barrier obtained from the data in Fig. 2c is compared with the one obtained from the CNT calculation (orange line and axis) with typical assumptions of GO characteristics (see Methods). Data shown in paler colours ($L\Delta T < 200$ nm K) correspond to nucleation on the water/substrate interface. Inset, the free-energy barriers in Fig. 4a are compared with those from the CNT calculation (orange). The error bars of the calculated parameters are calculated according to the error propagation formulae. **c**, Schematic illustrations of the shape of the critical ice nucleus when the size of GO nanosheet is smaller or larger than the critical ice nucleus diameter $2R_c$. ψ and θ are the apparent contact angles of the sphere-cap ice nucleus with the nanosheet plane.

surfaces anchored with nanosized GOs) can alter a surface's ability to control ice formation, which provides a strategy for the design of anti-icing surface materials[30].

Online content

Any methods, additional references, Nature Research reporting summaries, source data, extended data, supplementary information, acknowledgements, peer review information; details of author contributions and competing interests; and statements of data and code availability are available at https://doi.org/10.1038/s41586-019-1827-6.

1. Sosso, G. C. et al. Crystal nucleation in liquids: open questions and future challenges in molecular dynamics simulations. *Chem. Rev.* **116**, 7078–7116 (2016).
2. Gallo, P. et al. Water: a tale of two liquids. *Chem. Rev.* **116**, 7463–7500 (2016).
3. Zhang, Z. & Liu, X. Y. Control of ice nucleation: freezing and antifreeze strategies. *Chem. Soc. Rev.* **47**, 7116–7139 (2018).
4. Kiselev, A. et al. Active sites in heterogeneous ice nucleation—the example of K-rich feldspars. *Science* **355**, 367–371 (2017).
5. He, Z., Liu, K. & Wang, J. Bioinspired materials for controlling ice nucleation, growth, and recrystallization. *Acc. Chem. Res.* **51**, 1082–1091 (2018).
6. Moore, E. B. & Molinero, V. Structural transformation in supercooled water controls the crystallization rate of ice. *Nature* **479**, 506–508 (2011).
7. Matsumoto, M., Saito, S. & Ohmine, I. Molecular dynamics simulation of the ice nucleation and growth process leading to water freezing. *Nature* **416**, 409–413 (2002).
8. Fitzner, M., Sosso, G. C., Pietrucci, F., Pipolo, S. & Michaelides, A. Pre-critical fluctuations and what they disclose about heterogeneous crystal nucleation. *Nat. Commun.* **8**, 2257 (2017).
9. Pereyra, R. G., Szleifer, I. & Carignano, M. A. Temperature dependence of ice critical nucleus size. *J. Chem. Phys.* **135**, 034508 (2011).
10. Pradzynski, C. C., Forck, R. M., Zeuch, T., Slavicek, P. & Buck, U. A fully size-resolved perspective on the crystallization of water clusters. *Science* **337**, 1529–1532 (2012).
11. Xiao, Q. et al. What experiments on pinned nanobubbles can tell about the critical nucleus for bubble nucleation. *Eur. Phys. J. E* **40**, 114 (2017).
12. Lupi, L., Peters, B. & Molinero, V. Pre-ordering of interfacial water in the pathway of heterogeneous ice nucleation does not lead to a two-step crystallization mechanism. *J. Chem. Phys.* **145**, 211910 (2016).
13. Cabriolu, R. & Li, T. Ice nucleation on carbon surface supports the classical theory for heterogeneous nucleation. *Phys. Rev. E* **91**, 052402 (2015).
14. Lupi, L. et al. Role of stacking disorder in ice nucleation. *Nature* **551**, 218–222 (2017).
15. Russo, J., Romano, F. & Tanaka, H. New metastable form of ice and its role in the homogeneous crystallization of water. *Nat. Mater.* **13**, 733–739 (2014).
16. Palmer, J. C. et al. Metastable liquid–liquid transition in a molecular model of water. *Nature* **510**, 385–388 (2014).

17. Fletcher, N. H. Size effect in heterogeneous nucleation. *J. Chem. Phys*. **29**, 572–576 (1958).
18. Welti, A., Lüönd, F., Stetzer, O. & Lohmann, U. Influence of particle size on the ice nucleating ability of mineral dusts. *Atmos. Chem. Phys*. **9**, 6705–6715 (2009).
19. Liou, Y. C., Tocilj, A., Davies, P. L. & Jia, Z. C. Mimicry of ice structure by surface hydroxyls and water of a beta-helix antifreeze protein. *Nature* **406**, 322–324 (2000).
20. Garnham, C. P., Campbell, R. L., Walker, V. K. & Davies, P. L. Novel dimeric beta-helical model of an ice nucleation protein with bridged active sites. *BMC Struct. Biol*. **11**, (2011).
21. Liu, K. et al. Janus effect of antifreeze proteins on ice nucleation. *Proc. Natl Acad. Sci. USA* **113**, 14739–14744 (2016).
22. Whale, T. F., Rosillo-Lopez, M., Murray, B. J. & Salzmann, C. G. Ice nucleation properties of oxidized carbon nanomaterials. *J. Phys. Chem. Lett*. **6**, 3012–3016 (2015).
23. Häusler, T. et al. Ice nucleation activity of graphene and graphene oxides. *J. Phys. Chem. C* **122**, 8182–8190 (2018).
24. Lupi, L., Hudait, A. & Molinero, V. Heterogeneous nucleation of ice on carbon surfaces. *J. Am. Chem. Soc*. **136**, 3156–3164 (2014).
25. Zheng, Y., Su, C., Lu, J. & Loh, K. P. Room-temperature ice growth on graphite seeded by nano-graphene oxide. *Angew. Chem*. **52**, 8708–8712 (2013).
26. Roscoe, R. B. How does a rain drop grow? *Science* **129**, 123–129 (1959).
27. Koop, T., Luo, B. P., Tsias, A. & Peter, T. Water activity as the determinant for homogeneous ice nucleation in aqueous solutions. *Nature* **406**, 611–614 (2000).
28. Li, T. S., Donadio, D., Russo, G. & Galli, G. Homogeneous ice nucleation from supercooled water. *Phys. Chem. Chem. Phys*. **13**, 19807–19813 (2011).
29. Němec, T. Estimation of ice–water interfacial energy based on pressure-dependent formulation of classical nucleation theory. *Chem. Phys. Lett*. **583**, 64–68 (2013).
30. Eberle, P., Tiwari, M. K., Maitra, T. & Poulikakos, D. Rational nanostructuring of surfaces for extraordinary icephobicity. *Nanoscale* **6**, 4874–4881 (2014).

Article

Methods

Preparation of GOs of controlled sizes

The aqueous dispersion of GOs with a broad size distribution was procured from XFNANO Materials Tech (Nanjing). It was size-fractionated using a stirred cell (Millipore Amicon) with an Ultracel membrane inside it under a pressure of about 0.4 MPa. GOs of various sizes can be obtained by using Ultracel membranes with molecular weight cut-offs of 1 kDa, 50 kDa, 100 kDa, 300 kDa and 500 kDa, and the 0.1-μm microfiltration membrane. Specifically, six GO fractions were obtained. The first fraction (<1 kDa) is the filtrate of the 1 kDa membrane (not shown). The other fractions were obtained by (for example) filtering commercial GOs through a membrane with a 50 kDa cut-off, and then removing small GOs in the filtrate by allowing them to pass through a membrane with a 1 kDa cut-off, retaining only the larger ones (Fig. 1d); and similarly obtaining filtered products of the 50 kDa and 100 kDa membranes (Fig. 1e); 100 kDa and 300 kDa membranes (Fig. 1f); 300 kDa and 500 kDa membranes (Fig. 1g); and 500 kDa and 0.1 μm membranes (Fig. 1h), respectively. The GO fraction obtained was kept in water and stored at 4 °C in a refrigerator when not in use.

The mass concentrations of these GO aqueous dispersions were measured by weighing the solid content of GO in a fixed volume of the dispersion. Specifically, a coverslip was first weighed by an analytical balance (with the accuracy of 0.01 mg); then a fixed volume (such as 500 μl) of dispersion was carefully dripped on the coverslip and was dried in an oven. The coverslip with the dried GO was further weighed after it was cooled to room temperature, and the dry GO mass was obtained from the mass difference. Every concentration was measured at least three times for the mean. Afterwards, GO dispersions with desired concentrations were prepared by diluting these mother dispersions with ultrapure water (18.2 MΩ cm) provided by Millipore Milli-Q apparatus and filtered through the 0.22-μm membrane.

Estimation of GO molar concentrations

Molar concentrations of GO aqueous dispersions were estimated from their mass concentrations and the molar mass of GOs. First, the molecular weight of GOs of different sizes was estimated based on a previous well-accepted structural model of GO[31,32]; that is, GO with a size of 2.13 nm × 2.46 nm has a chemical formula of $C_{240}O_{24}(OH)_{24}(COOH)_{12}$. Therefore, the molar mass of a GO nanosheet of unit size $M_{GO,A}$ was calculated as $M_{GO,A} = M[\text{GO model}]/A[\text{GO model}]$. Here $M[\text{GO model}]$ and $A[\text{GO model}]$ are the molar mass and area (in nm^2) of $C_{240}O_{24}(OH)_{24}(COOH)_{12}$, respectively. As revealed by the TEM imaging, the shape of the GOs is nearly circular. The average molar mass of GOs with a certain average lateral size $M_{GO,L}$ was then calculated as $M_{GO,L} = \pi(L/2)^2 \times M_{GO,A}$. Here L is the average lateral dimension of GO measured from TEM images. Based on the average molar mass, the molar concentration of GO aqueous dispersion with a known mass concentration was estimated.

Preparation of GO samples with decreasing degree of oxidation

To obtain GOs with the same size but decreasing degrees of oxidation, the prepared GOs of controlled sizes were deoxidated by the facile alkali treatment method[33,34]. Specifically, the GO aqueous dispersion (typically 0.2 mg ml⁻¹ and 20 ml) with GOs within a specific size range was placed into vials in triplicate. The pH values of two of these dispersions were adjusted to 10 and 12 with 1 mol l⁻¹ NaOH solution, respectively. The third dispersion was untreated. Then the three dispersions were stirred for 12 h. Subsequently, these three samples were purified to remove NaOH and other small molecules using Millipore Amicon stirred cell with an Ultracel membrane (molecular weight cut-off, 1 kDa) inside it. The purification processes were repeated three times to ensure that all impurities were removed. Finally, we added the required amount of ultrapure water according to the desired concentration into the Millipore Amicon stirred cell, to obtain GO aqueous dispersions with the

same size range but different degrees of oxidation. The GOs without alkali treatment and with the alkali treatments at pH = 10 and 12 were named R0, R1 and R2, respectively. See Supplementary Figs. 6, 7, 8 and 9 for the elemental content, hydrodynamic diameter, zeta potential and dispersibility characterizations.

Anchoring of GOs on silicon wafer surfaces

GOs were anchored on the Si wafer surface via the electrostatic adsorption between the amino groups of aminopropyltriethoxysilane (APTES) on the substrate and carboxyl groups of GOs. First, the Si wafer surface was modified with APTES[35]. The Si wafer surface covered with APTES was soaked in the GO aqueous dispersion (2 μmol l⁻¹) for 12 h, and then ultrasonically cleaned in ethanol (5 s, 100 W, 40 kHz) and rinsed with ultrapure water, followed by flushing with nitrogen gas. The obtained sample was denoted Si–APTES–GO.

Preparation of laponite aqueous dispersion

Laponite RD (chemical formula $Na^+_{0.7}[(Si_8Mg_{5.5}Li_{0.3})O_{20}(OH)_4]^{-0.7}$) with a purity over 99% was a gift from Huizhi Fine Chemical (Sihong). Laponite powder (total 2.25 g) was added stepwise into 225 ml ultrapure water at 65 °C under vigorous stirring. The amount each time added was about 0.2 g. Note that no additional laponite powder was added to the water until the dispersion turned clear. The entire addition period was about 1 h.

The preliminarily dispersed laponite was then filtered through a membrane filter with a pore diameter of 1 μm. The filtrate was then treated with ultrasonication for 3 h (40 kHz, 300 W, KQ-300DE ultrasonic cleaner, Kunshan Ultrasonic Instruments). After this, the laponite aqueous dispersion was poured into a stirred cell (Millipore Amicon) with an Ultracel membrane with 100-kDa cut-off inside it and filtrated under a pressure of about 0.4 MPa to remove the smaller nanosheets and other small molecules. Finally, ultrapure water was added to obtain 140 ml laponite aqueous dispersion. The mass concentration was measured by weighing the dry laponite mass in the dispersion of a fixed volume, and the molar concentration was then estimated based on the density (2.5 g cm⁻³) and size (obtained by analysing AFM images, Extended Data Fig. 6) of laponite. The newly prepared laponite aqueous dispersion was used for ice nucleation measurements within 2 days to avoid the formation of possible aggregates.

Characterizations of GOs

The sizes of various GO samples were measured based on the images taken with the transmission electron microscopy (TEM, JEM-2100F, JEOL). AFM (Multimode 8, Bruker) was also used to investigate the morphology and thickness of GOs. The morphology of GOs in water was further examined by cryo-TEM (Tecnai Arctica, FEI). Specifically, the vitrified specimen was prepared in a closed chamber with 100% relative humidity and fixed temperature of 4 °C. First, a 3-μl droplet of GO aqueous dispersion (0.4 mg ml⁻¹) was dripped onto a perforated carbon film-supported grid held by tweezers and pre-equilibrated in the chamber. Excess dispersion was removed by blotting with a piece of filter paper for 4 s, producing a thin liquid film spanning the holes of the grid. The grid was then plunged into the liquid nitrogen to create the vitrified sample. Micrographs were recorded by a K2 Summit direct electron detector (Gatan) at a nominal magnification of 120,000×. Raman spectra were taken on a Raman spectrometer equipped with a 532-nm laser (LabRAM HR Evolution, HORIBA). The elemental content and chemical bonding were determined by X-ray photoelectron spectroscopy (XPS, ESCALab220i-XL, Thermo Fisher Scientific). Peak deconvolution with Gaussian curves of elements was accomplished by XPSPEAK 4.1 software. Zeta potentials of GO aqueous dispersions were measured by a Malvern Zetasizer (Nano ZS90, Malvern). Hydrodynamic diameters of various GO samples were measured by dynamic light scattering spectrometer (ALV/SP-125, ALV) equipped with a multi-τ digital time correlator (ALV-5000) and a He–Ne laser (22 mW, λ = 632.8 nm).

The measurements were conducted at a scattering angle of 90°. All dispersions were filtrated through syringe filters with pore size of 0.45 μm before the measurements. All the measurements were performed at 25.00 ± 0.01 °C. The data obtained by dynamic light scattering reflect the size change of different GO fractions. Solid-state ^{13}C high-power proton decoupling NMR spectra were acquired on a Bruker Avance III-400 spectrometer (100.38 MHz ^{13}C, 399.16 MHz ^{1}H) after excitation with a 30° pulse and with a recycle delay of 15 s. A total of 15,360 scans were accumulated to obtain good signal-to-noise ratio. A 4-mm rotor and a spinning rate of 12 kHz were used. Peak deconvolution was accomplished by MestReNova software to separate the crowded peak.

Ice nucleation measurement

The ice nucleation temperature T_{IN} and delay time were measured in a closed cell consisting of a rubber O-ring (height 2.0 mm, inner diameter 15 mm) sandwiched between two optical microscope cover glasses. Inside the closed cell, about 10 droplets of water or GO aqueous dispersions were placed atop a circular cover glass (Linkam 3930) using transferpettes. To minimize the influence of the substrate on the ice nucleation and to ensure that the freezing events of each water droplet are independent (Extended Data Fig. 2a), the circular cover glass was coated in advance with a silicone oil thin film about 40 μm thick (AR 1000 from Aldrich, which has a higher density than that of water, 1.09 g ml^{-1} at 20 °C)[36]. The entire preparation of the sample cell was carried out in a Class II Type A2 biosafety cabinet to avoid contamination. All the water used in the experiments was ultrapure water. The closed cell is small enough (0.35 cm[3]) that the water vapour in the closed cell can be approximated to be 100% relative humidity. Then the closed cell was placed atop a cryostage (Linkam LTS420) and cooled at a rate of 1, 5, 10 or 15 °C min^{-1}.

The formation of ice was observed through an optical microscope (Nikon AZ100) equipped with a digital camera (Nikon DS-Ri1). The temperature at which a sudden change in the opacity of water droplets was first observed was identified as T_{IN}. One-way analysis of variance (ANOVA) was also performed on the T_{IN} data of water droplets containing GOs with a series of sizes for statistical significance (significance level of difference of the mean is 0.05; see Supplementary Section PS2).

For GOs anchored on Si wafer surfaces, T_{IN} was measured in a similar way. The difference was that we replaced the silicone oil coated cover glass with the sample to be tested and then pure water droplets were placed atop the Si wafer surfaces anchored with GOs. The number of nucleation sites was tuned by the contact area of the water droplets with the substrate, achieved by changing the volumes of the water droplets. Every sample with water droplets atop was photographed by an optical microscope equipped with a digital camera, and then the images were analysed by the NIS-Elements BR software to obtain the contact area of the water droplet with the substrate.

The delay time of ice nucleation at a certain temperature was measured as the time elapsed from the time when the substrate was cooled to a target temperature to the time when the ice nucleation occurred. Estimate of mean delay time of ice nucleation was as follows. We independently measured the ice nucleation delay time N times in our experiments, and the longest waiting time was $t_0 = 9,000$ s. Within 9,000 s, we found m nucleation events at $t_1, t_2, ..., t_m$, respectively, and the remaining $N - m$ measurements did not have nucleation events (N varies from 20 to 150 to ensure that m is typically not less than 10). We have an estimator of the delay time (the mean waiting time), $t_D = (1/m)[\sum_{i=1}^{m} t_i + \sum_{j=m+1}^{N} t_0]$. We applied the jackknife resampling technique to obtain the error of the estimator of the delay time.

The free-energy barrier from the ice nucleation temperature and the mean delay time

Generally, the ice nucleation rate, $J(T) = nK(T)\exp[-\Delta G^*/(k_B T)]$, determines the temperature of ice nucleation in the cooling experiments and the mean delay time of ice nucleation t_D at each specific temperature. Here n is the number of ice nucleation active sites (GOs) in water droplets; $K(T)$ is the kinetic prefactor; ΔG^* is the major (highest) free-energy barrier of ice nucleation (if multiple barriers exist); k_B is the Boltzmann constant.

The ice nucleation temperature. When water droplets are slowly cooled, the probability that an ice nucleation event happens for the first time at temperature T is $P(T) = (1/\alpha)J(T)\exp[(1/\alpha)\int^T J(T')dT']$. Here $\alpha = |dT/dt|$ is the cooling rate. When T decreases, the ice nucleation rate $J(T)$ quickly increases; but the exponential term quickly decreases; thus $P(T)$ is significantly non-zero only in a small supercooling temperature range, corresponding to the detected nucleation temperature. Within a small temperature range, we approximately have $J(T) \approx nK\exp(-\Delta\bar{G}^*)$, where K is constant, and $\Delta\bar{G}^* = \Delta G^*/(k_B T)$.

We can define the mean temperature $\bar{T} = \int P(T)dT$, and the temperature T_f^x, at which the cumulative probability of ice nucleation is x, satisfies $\int^{T_f^x} (J(T)/\alpha)dT = \ln(1-x)$. Usually we set $x = 0.5$, then $T_f^{0.5}$ is the median temperature of ice nucleation. The mean temperature and the median temperature $T_f^{0.5}$ do not equal each other, but their difference is found to be very small in the current experiments (Supplementary Fig. 13). Thus, we usually do not distinguish them if not explicitly mentioned.

The relationship between $T_f^{0.5}$ and n satisfies the equation $J(T_f^{0.5}) = \alpha(\ln 2)\frac{d\ln n}{dT_f^{0.5}}$. Since $\frac{d}{dT}\ln n(T)$ usually varies much more slowly with T in comparison with $J(T)$, we approximate it as a constant; thus we have $J(T_f^{0.5})$ being a constant when α is fixed. We can then determine the dependence of $T_f^{0.5}$ on n.

Therefore, we have $\ln n(T) \approx \Delta\bar{G}^*(T) + c'$. Here c' is almost a constant when $\Delta T > \Delta T_L$, but changes with T when $\Delta T \le \Delta T_L$, since $\frac{d}{dT}\ln n(T)$ is a constant when $\Delta T > \Delta T_L$, but changes rapidly with T when $\Delta T \le \Delta T_L$.

The delay time of ice nucleation. The distribution of the delay times of ice nucleation at a fixed temperature is $P(t) = J(T)\exp[-tJ(T)]$. Thus, the mean delay time is $t_D = J(T)^{-1} = n^{-1}K^{-1}\exp(\Delta\bar{G}^*)$ where K is the prefactor of the nucleation rate. Then we have $\ln\tau(T) \approx \Delta\bar{G}^*(T) + c$ with constant c. Here $\tau(T) = nt_D(T; n)$ is independent of the number of GOs, n, since t_D is inversely proportional to n.

When $\Delta T > \Delta T_L$ and within a small range of temperature, we found that both $\ln n(T)$ and $\ln\tau(T)$ are linearly related to $1/\Delta T^2$ with different additional constants, consistent with CNT. Thus we fitted the free-energy barrier by $\Delta\bar{G}^* \propto 1/\Delta T^2$ from the curves $\ln n(T)$ and $\ln \tau(T)$, as shown in Fig. 4a.

Ice nucleation on gold nanoparticles

We also investigate the ice nucleation of water droplets containing gold nanoparticles of controlled size and show the results in Supplementary Section PS5. Abrupt transition in the activity of the nanoparticles in facilitating ice nucleation occurs at a critical size of gold nanoparticle.

Theoretical calculation of free-energy barrier of ice nucleation on finite-sized GOs

Based on CNT, on sufficiently large GO surfaces, the free-energy barrier $\Delta\bar{G}^* = \Delta\bar{G}_{het}^* = \bar{a}/\Delta T^2$, where $\bar{a} = \frac{16\pi\gamma^3}{3|\Delta S|^2 k_B T}f(\theta)$ is approximately constant if the temperature is limited within a small range. Here γ is the surface tension of the ice–water interface, ΔS is the entropy difference between ice and water at the equilibrium melting temperature, and $f(\theta)$ describes the capability of sufficiently large GOs in facilitating ice nucleation.

When the size of GOs is comparable with that of the critical ice nucleus, the free-energy barrier $\Delta\bar{G}^*(L; \Delta T) = \Delta\bar{G}_{het}^*(\Delta T)\hat{g}(l)$. Here $\hat{g}(l)$ is a function of the dimensionless size of GOs,

Article

$l \equiv L/(2R_c)$ $(= L\Delta T/x_c \equiv \Delta T/\Delta T_L)$, and $R_c = 2\gamma/(|\Delta S|\Delta T)$ is the radius of the critical ice nucleus. $x_c = 4\gamma/|\Delta S|$ is approximately constant, and $\Delta T_L = x_c/L$.

The function $\hat{g}(l)$ can be calculated by modelling the shape of GOs (see Supplementary Section PS6). Here we suppose that the GO is a thin flat disk with a smooth semi-circular edge. As shown in Extended Data Fig. 8a, $\hat{g}(l)$ has an abrupt transition at $l = l_c \approx 1$. The result is not sensitive to the detailed shape of nanosheet as discussed below. The free-energy barrier is determined by the shape of critical ice nucleus under the requirement of minimizing its total interfacial free energy, involving that of its GO-covered surface and that of the GO-uncovered surface (that is, the interface between water and ice). For large GOs, it results in a critical ice nucleus in the shape of a sphere-cap atop the flat surface of GO, with radius R_c regardless of GO, and the contact angle θ determined by the Young's equation, $\gamma\cos\theta = \gamma_{WG} - \gamma_{IG}$. Here γ_{WG} and γ_{IG} are the surface energy of the water–GO and ice–GO interfaces, respectively. For small GOs, it forces a complete covering of the ice nucleus on the flat surface of GO to minimize the interfacial free energy of the GO-covered surface of ice nucleus, $(\gamma_{IG} - \gamma_{WG})S_{IG} = (-\gamma\cos\theta)S_{IG}$ with $S_{IG} \approx (\pi/4)L^2$, and a partial spherical surface of the GO-uncovered water/ice surface of the ice nucleus. Thus, the critical ice nucleus is a sphere-cap pinned at the edge of GO, with approximately the same radius R_c, and a large contact angle ψ, with $\cos\psi \approx -\sqrt{1-l^2}$, almost regardless of the details of the edge of the GO nanosheets. Therefore, the free-energy barrier is $\Delta G^* = \gamma S_{WI} - (\gamma\cos\theta)S_{IG} - |\Delta\mu|V$. Here S_{WI} and V are the area of the water–ice interface and the volume of the critical ice nucleus, respectively; $S_{WI} \approx 2\pi R_c^2(1 - \cos\psi)$ and $V \approx (4\pi/3)R_c^3 f(\psi)$. Then $\hat{g}(l) \approx [1/f(\theta)][f(\psi) - (3/4)l^2|\cos\psi - \cos\theta|]$ has a similar abrupt change when $l = l_c \approx 1$.

We illustrate the change in shape of the ice nucleus during its growth on GO nanosheet. As shown in Extended Data Fig. 8b, when $L \approx 2R_c$, the first critical ice nucleus with radius R_c forms on the nanosheet surface because of thermodynamic fluctuation; and then the ice nucleus spontaneously grows until it meets the edge of the nanosheet. After that, the growing ice nucleus increases its contact angle and first decreases, then increases its radius because it is pinned at the edge of the nanosheet. This leads to the second critical ice nucleus which has almost the same radius R_c, but a larger contact angle. Extended Data Fig. 8c shows the changes of the free energy, contact angle and radius of ice nucleus with volume.

Comparison between the experimental and theoretical free-energy barriers

From the data shown in Fig. 2c, we calculate $\hat{g}(l) = \Delta T^2(L\Delta T; C)/\Delta T_\infty^2(C)$, where $l = L\Delta T/x_c$ with $x_c = 200$ nm K, and $\Delta T_\infty(C) = T_m - T_{IN,\infty}(C)$ for each concentration of GO, C. From the data in Fig. 4a, we get $\hat{g}(l) = \Delta G^*(\Delta T)/\Delta G_{het}^*(\Delta T)$ (where the subscript 'het' means heterogeneous nucleation), with $l = \Delta T/\Delta T_L$ for GOs of various sizes by using the experimental value of their ΔT_L, respectively, and the free-energy barrier of the normal heterogeneous nucleation on an infinite plane substrate, $\Delta G_{het}^*(\Delta T) \propto 1/\Delta T^2$, when ΔT is near ΔT_L. The comparison is shown in Fig. 4b of the main text.

Data availability

The data that support the findings of this study are available from the corresponding author upon reasonable request.

31. Tu, Y. et al. Destructive extraction of phospholipids from *Escherichia coli* membranes by graphene nanosheets. *Nat. Nanotechnol.* **8**, 594–601 (2013).
32. Geng, H. et al. Graphene oxide restricts growth and recrystallization of ice crystals. *Angew. Chem.* **56**, 997–1001 (2017).
33. Rourke, J. P. et al. The real graphene oxide revealed: stripping the oxidative debris from the graphene-like sheets. *Angew. Chem.* **50**, 3173–3177 (2011).
34. Fan, X. et al. Deoxygenation of exfoliated graphite oxide under alkaline conditions: a green route to graphene preparation. *Adv. Mater.* **20**, 4490–4493 (2008).
35. Bai, G. et al. Self-assembly of ceria/graphene oxide composite films with ultra-long antiwear lifetime under a high applied load. *Carbon* **84**, 197–206 (2015).
36. Du, N., Liu, X. Y. & Hew, C. L. Ice nucleation inhibition—mechanism of antifreeze by antifreeze protein. *J. Biol. Chem.* **278**, 36000–36004 (2003).

Author contributions G.B., X.Z. and J.W. conceived the project and designed the experiments. G.B., D.G. and Z.L. performed the experiments. G.B., D.G., Z.L., X.Z. and J.W. analysed the data. G.B., D.G., X.Z. and J.W. prepared the manuscript.

**Competing interests** The authors declare no competing interests.

Additional information
Supplementary information is available for this paper at https://doi.org/10.1038/s41586-019-1827-6.
Correspondence and requests for materials should be addressed to X.Z. or J.W.
**Peer review information** *Nature* thanks Niall English, Christoph Salzmann and the other, anonymous, reviewer(s) for their contribution to the peer review of this work.
**Reprints and permissions information** is available at http://www.nature.com/reprints.
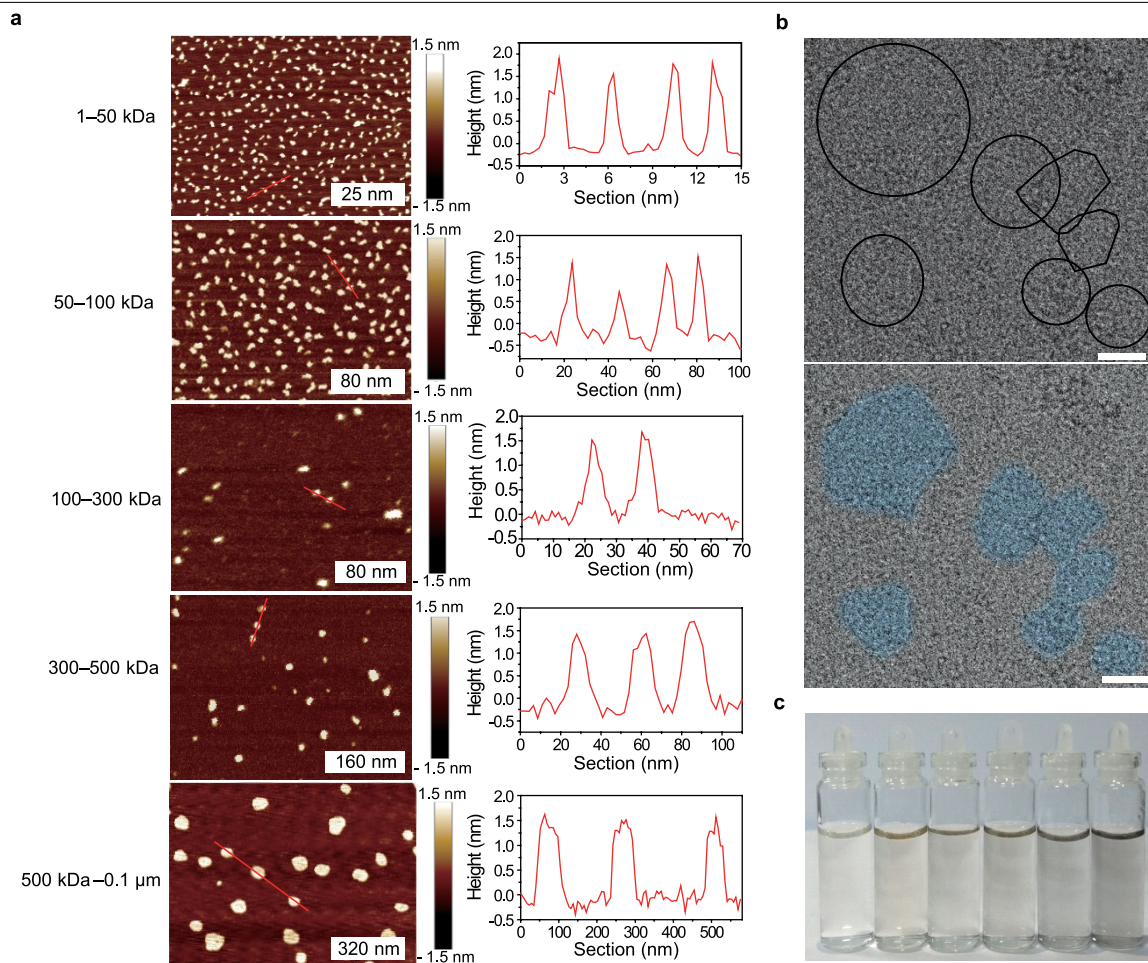
Extended Data Fig. 1 | Characterizations of GOs of controlled sizes. a, AFM images of GOs of five controlled sizes and the corresponding height profiles along the lines marked. **b**, Cryo-TEM images of GOs of various sizes before size fractionation, showing the shape of the GOs in water. The upper image is the original; the lower panel is the image with enhanced contrast by colouring the GO domains to help the visibility. Scale bar, 10 nm. **c**, Photographs of 0.04 mg ml^{-1} GO aqueous dispersions. From left to right, the average lateral sizes of GO are <1 kDa, 3 nm, 8 nm, 11 nm, 21 nm and 50 nm, respectively. All the GO aqueous dispersions are clear and transparent, indicating the good dispersibility of various-sized GOs in water.

a

b
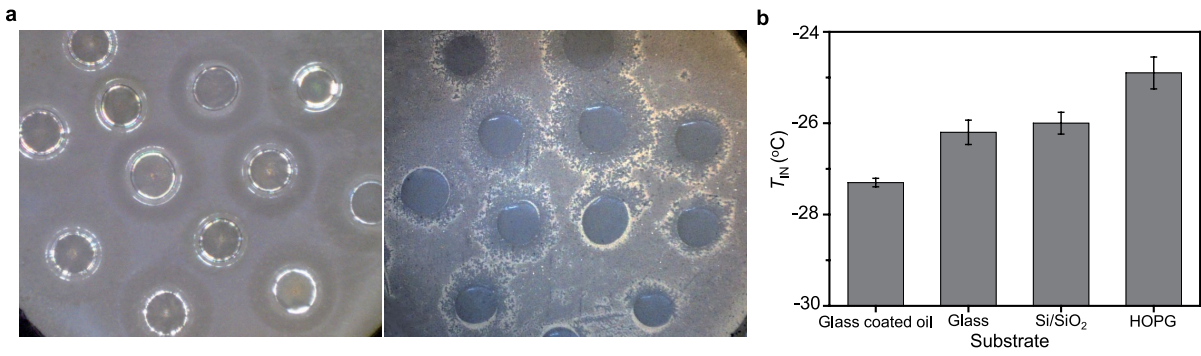
**Extended Data Fig. 2 | Influence of the substrate on the ice nucleation measurement. a**, Optical microscopic images of frozen water droplets on glass coverslip coated with a thin layer of silicone oil (left) and without silicone oil (right) during the ice nucleation assays. The other experimental conditions for these two images are identical (see Methods). The frozen water droplets on a glass coverslip coated with a thin oil film are independent. In contrast, on the glass coverslip without a thin oil film, the freezing events of the water droplets are not independent. **b**, Ice nucleation temperatures of water droplets on glass coated with silicone oil, glass without oil, silicon wafer and highly oriented pyrolytic graphite (HOPG). Data are means ±s.e.m. For each mean, the total number of the measurements is not less than 50. The volume of the water droplet is 0.2 µl. Cooling rate, 5 °C min^{-1}. T_{IN} of water droplets on different substrates shows different values, suggesting that the ice nucleation is initiated at the water/substrate interface.
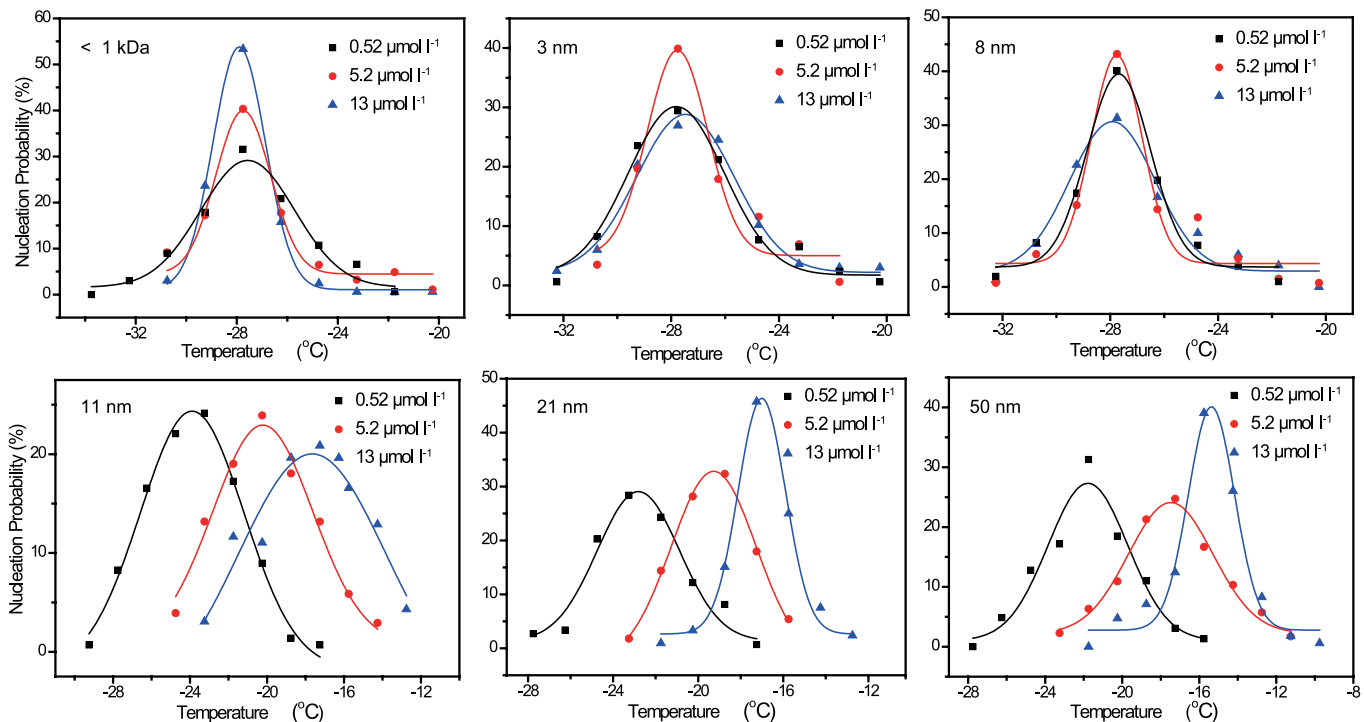
Extended Data Fig. 3 | Ice nucleation probability distribution of water droplets containing GOs of controlled sizes at three different concentrations. The distributions are fitted by Gaussian functions. For each distribution, the total number of ice nucleation measurements is about 150.

The results show that the change in concentration (from 0.52 to 13 μmol l⁻¹) of GOs with sizes smaller than 8 nm does not affect the T_{IN} of water droplets; however, T_{IN} increases with the concentration of GOs when the GO size is above 11 nm.
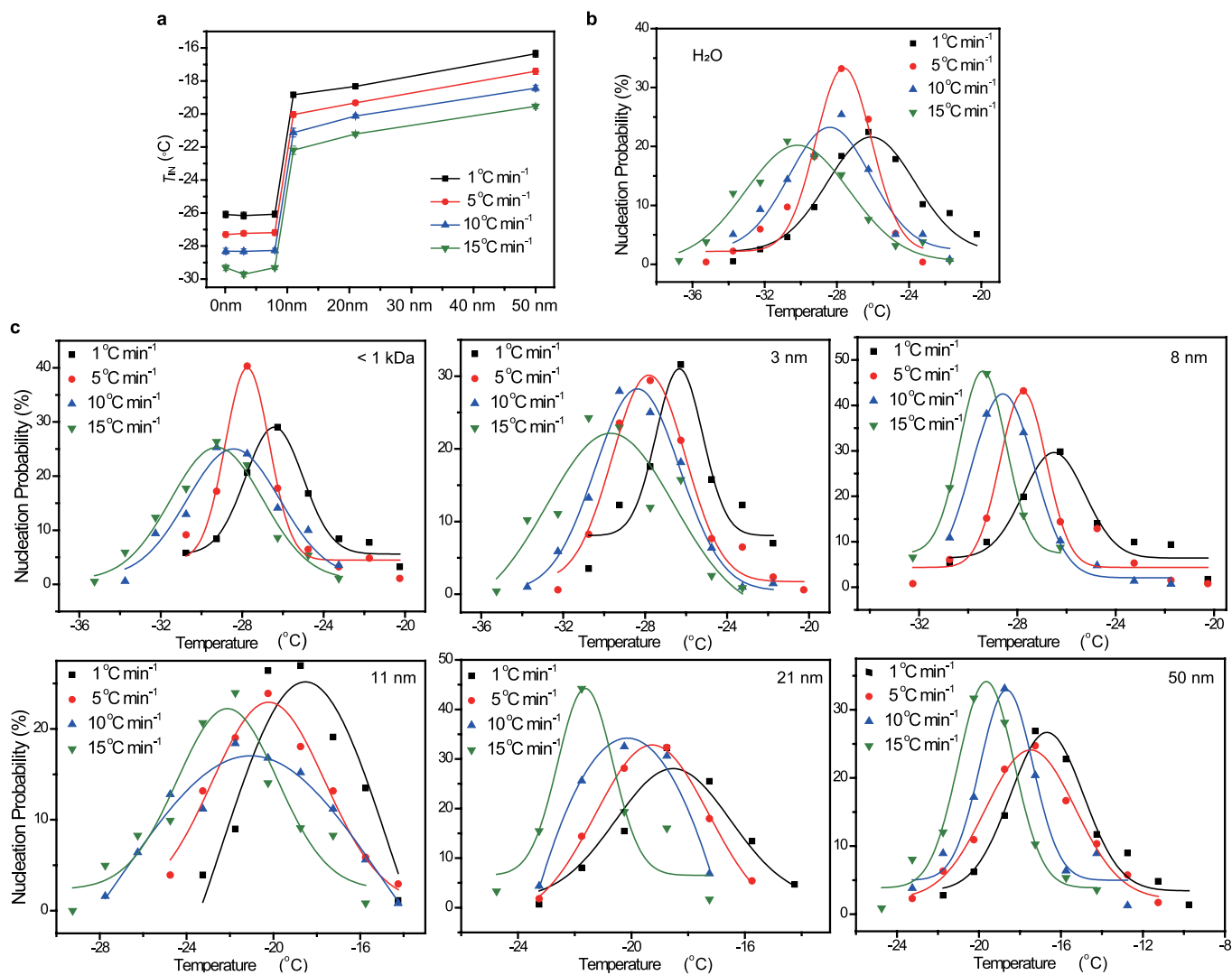
Extended Data Fig. 4 | Ice nucleation temperatures of droplets of GO aqueous dispersions at cooling rates ranging from 1 °C min⁻¹ to 15 °C min⁻¹. **a**, Cooling rate dependence of T_{IN} of water droplets containing GO samples of controlled sizes. Data are means ±s.e.m. For each mean, the total number of measurements is about 150. **b**, Ice nucleation probability distribution of the blank control (water droplets) at various cooling rates with Gaussian fitting. **c**, Ice nucleation probability distribution (Gaussian fitting) of water droplets containing GOs with a series of average lateral sizes at various cooling rates. For each distribution, the total number of measurements is about 150. The concentration of GO aqueous dispersion is 5.2 µmol l⁻¹. All the volumes of water droplets are 0.2 µl.
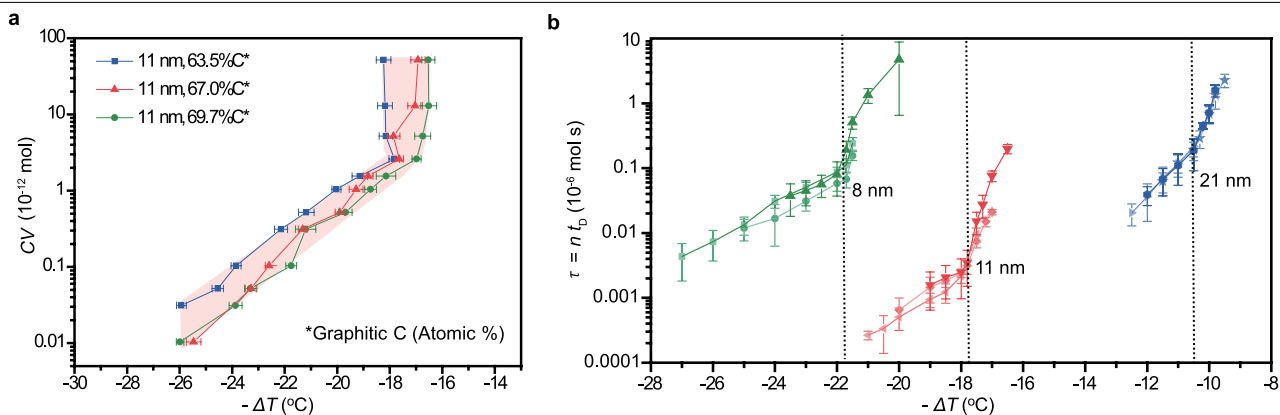
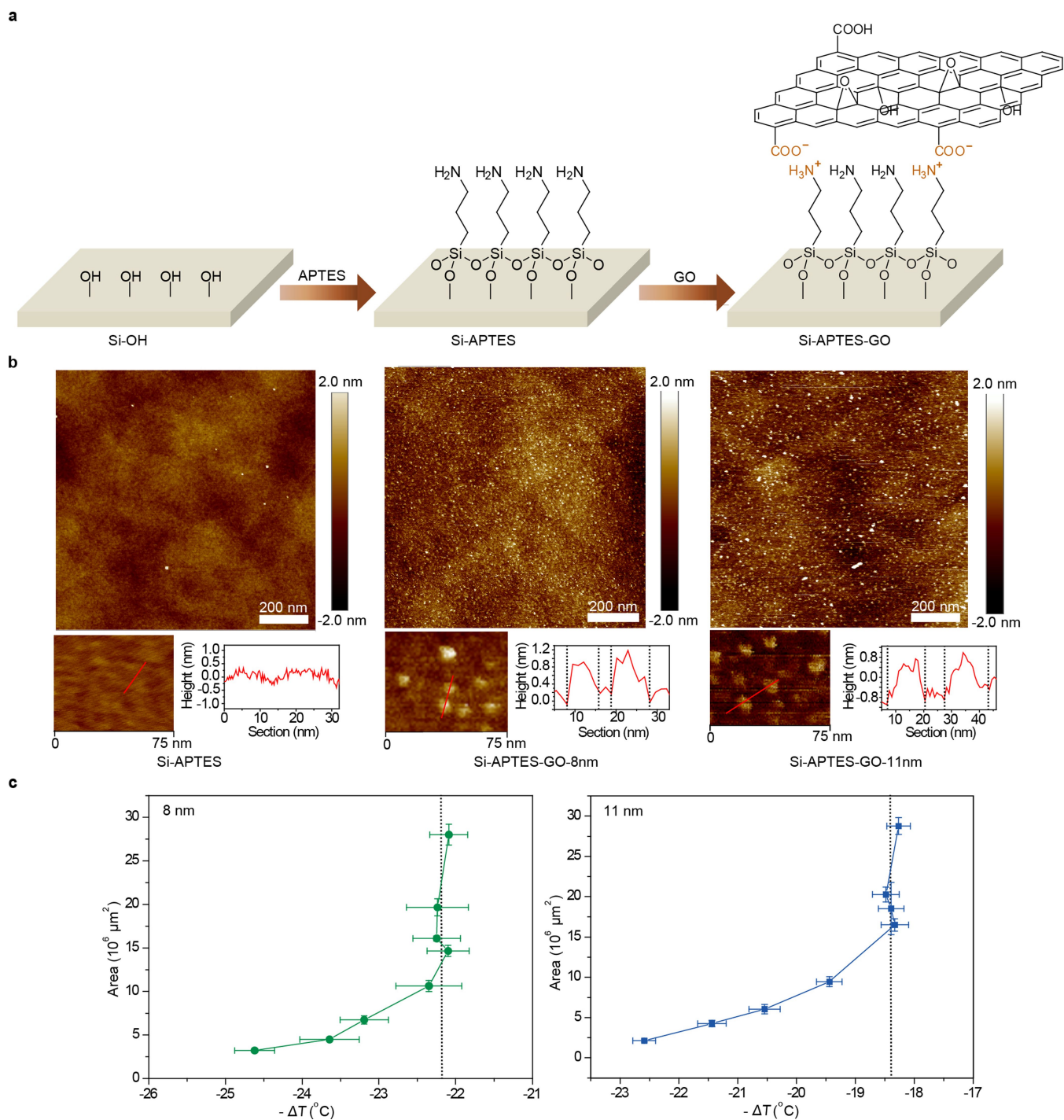**Extended Data Fig. 5 | The transitions of the ice nucleation activity of GOs.** **a**, The mean ice nucleation (supercooling) temperature $-\Delta T \equiv T_{\mathrm{IN}} - T_{\mathrm{m}}$ versus the number of GOs in the water droplet, $n = CV$ (for concentration, C and volume, V), for three degrees of oxidation of GOs with the same lateral size of 11 nm. Here the cooling rate is always 5 °C min^{-1}. Data are means ±s.e.m. For each mean, the total number of the measurements is about 50. **b**, The scaled delay time of ice nucleation of water droplets containing GOs, $\tau = nt_{\mathrm{D}}(T; n)$, versus ΔT. The three curves for each GO size come from different n (the same as Fig. 3b in the main text) and collapse into the same curve. Data are means; error bars are standard deviation estimated by the jackknife resampling technique. For each mean, the total number of measurements varies from 20 to 150 to ensure that the nucleation event number m is typically not less than 10 (see Methods).

a

b
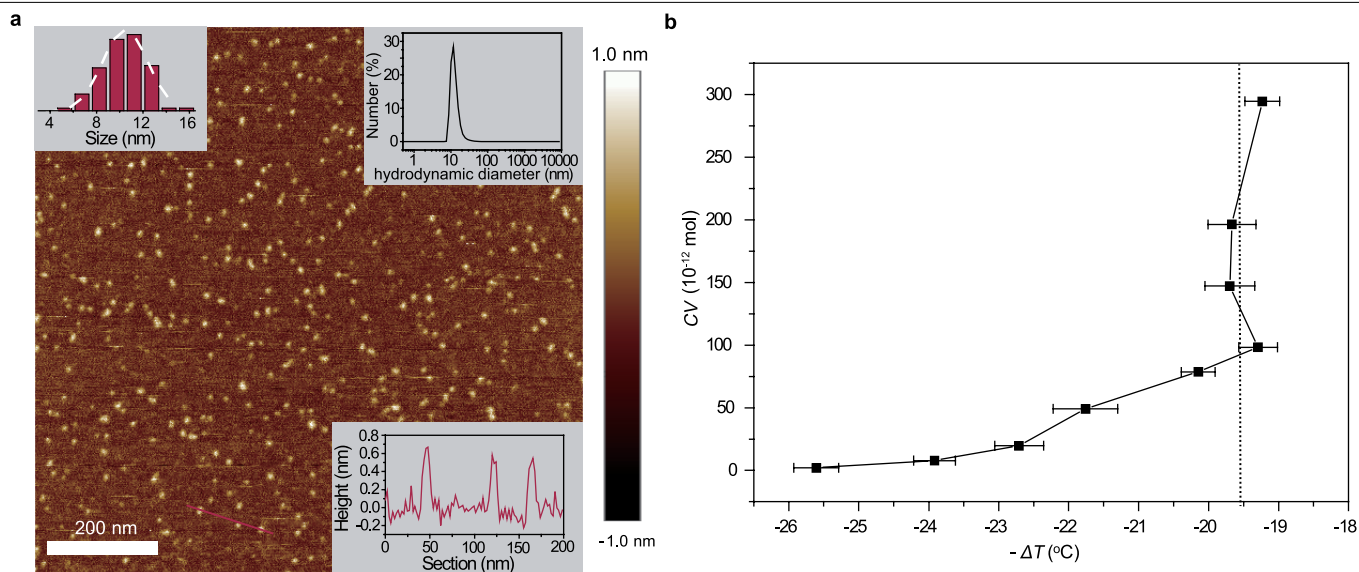
**Extended Data Fig. 6 | Characterization and ice nucleation activity of laponite. a**, AFM characterization of the prepared laponite. The insets show the lateral size distribution, the thickness and the hydrodynamic diameter of laponite. The size distribution is obtained by averaging the lateral sizes of more than 100 laponite nanosheets imaged by AFM. The hydrodynamic diameter of laponite nanosheets is measured by a Malvern Zetasizer. **b**, The ice nucleation (supercooling) temperature $-\Delta T \equiv T_{IN} - T_m$ versus the number of laponites contained in the water droplet (for concentration, C and volume, V). Here the cooling rate is always 5 °C min^{-1}. Data are means ±s.e.m. For each mean, the total number of the measurements is about 50.

Extended Data Fig. 7 | Characterization and ice nucleation temperature investigations of GOs anchored on silicon water surface. a, Schematic illustration showing the preparation process of the anchored GOs on Si wafer surfaces. **b**, AFM characterizations of the prepared surfaces without GOs and with GOs of controlled sizes. **c**, The ice nucleation (supercooling) temperature $-\Delta T \equiv T_{IN} - T_m$ versus the contact area between the water droplets and the surface to which the GOs are anchored. The contact area, measured by optical microscopy, is proportional to the number of nucleation active sites (see Methods). Here the cooling rate is always 5 °C min^{-1}. Data are means ±s.e.m. For each mean, the total number of measurements is about 50.
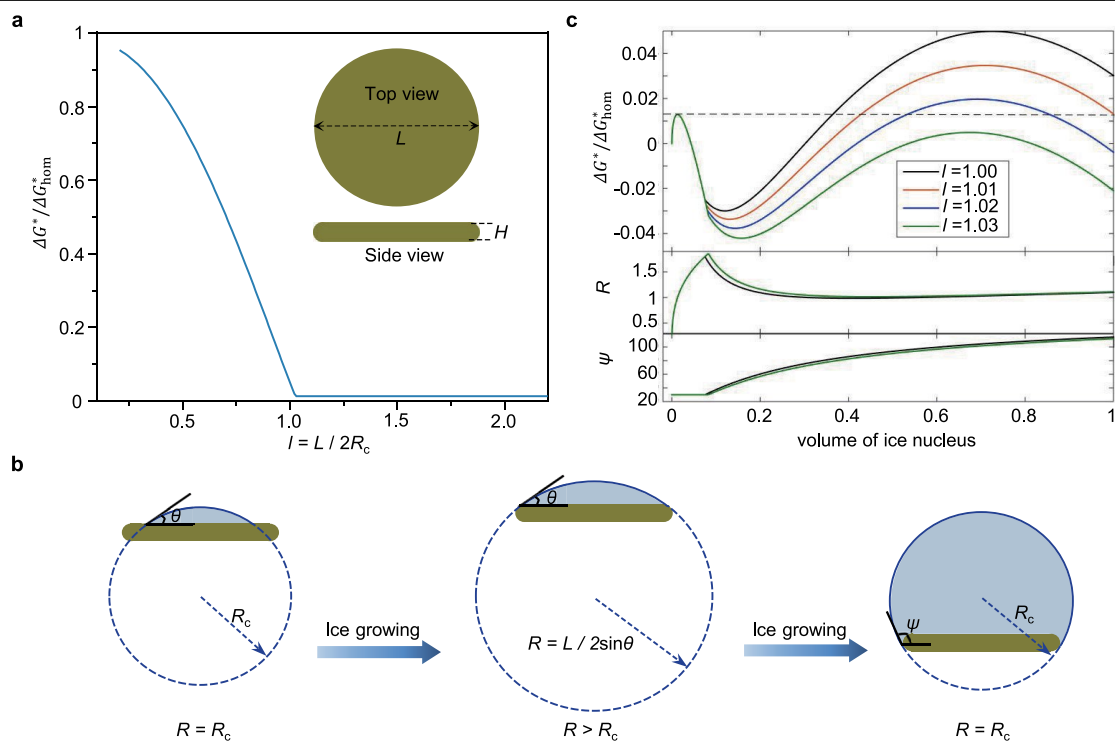
Extended Data Fig. 8 | Theoretical analysis of ice nucleation on finite-sized nanosheet. a, Free-energy barrier of ice nucleation on a thin-disk GO versus the normalized size of GOs. The inset shows the schematic illustration of thin-disk-shaped GOs with a smooth hemispherical edge. Its major diameter (lateral size) is L, and the thickness is H. **b**, Schematic diagram showing three typical shapes of ice nucleus on GO when $L \approx 2R_c$. The first and the third are the critical ice nuclei corresponding to two different free-energy barriers (see Methods).

c, The calculated dimensionless free energy, radius of ice nucleus (in units of R_c) and the apparent contact angle ψ versus the volume of ice nucleus (in units of $(4\pi/3)R_c^3$) on the thin-disk GO nanosheet when $L \approx 2R_c$. Here the dimensionless thickness of GO disk $h = H/2R_c = 0.1$, and θ (=30°) is the intrinsic contact angle between ice nucleus and the GO. The obtained results are not sensitive to these details of GO and the applied parameters (see Methods and Supplementary Section PS6).

Extended Data Table 1 | Summary of characterization of GOs of controlled sizes

Sample	< 1 kDa	1–50 kDa	50–100 kDa	100–300 kDa	300–500 kDa	500 kDa–0.1 µm
TEM diameter (mean ± s.d.) (nm)	N/A	2.63 ± 0.46	7.63 ± 1.54	10.91 ± 2.2	20.91 ± 4.41	49.75 ± 12.11
Hydrodynamic diameter (mean ± s.d.) (nm)	0.62 ± 0.05	2.80 ± 0.58	7.73 ± 1.15	14.36 ± 0.84	29.69 ± 6.49	68.34 ± 10.12
Zeta potential (mean ± s.d.) (mV)	N/A	- 24.0 ± 1.0	- 24.6 ± 2.0	- 24.0 ± 0.5	- 23.3 ± 2.7	- 21.5 ± 2.2
C/O atomic ratio	1.35	2.45	2.58	2.60	3.13	3.14
Graphitic C/oxidized C	1.48	1.54	1.57	1.67	1.85	2.01
Graphitic C (Atomic %)	59.6	60.7	61.1	62.8	64.9	66.8
C-O (Atomic %)	21.8	20.6	21.8	23.0	26.5	24.5
C=O/COOH (Atomic %)	18.6	18.7	17.1	14.2	8.6	8.7
I_D/I_G	1.19 ± 0.07	1.12 ± 0.01	1.05 ± 0.02	1.02 ± 0.01	1.01 ± 0.02	1.01 ± 0.03

The TEM diameter of each sample is obtained by averaging the lateral sizes of more than 100 GOs imaged by TEM. Hydrodynamic diameter and zeta potential for each sample are obtained by averaging three measurements. Hydrodynamic diameter and zeta potential distributions of GOs are shown in Supplementary Figs. 1 and 2. The carbon (C) content in different chemical states can be obtained from the area ratio of the sub-peaks in the C 1s core-level XPS spectra (Supplementary Fig. 3). I_D/I_G represents the intensity ratio of the D band to G band obtained from Raman spectroscopy (Supplementary Fig. 5) and is obtained by averaging three measurements.

Article

Extended Data Table 2 | Ice nucleation temperatures of water droplets containing GOs of controlled sizes and decreasing degrees of oxidation

C (μmol l^{-1})	3nm		8nm		11nm		21nm		50nm	
	Graphitic C (Atomic %)	T_{IN} (°C) (mean ± s.e.m.)	Graphitic C (Atomic %)	T_{IN} (°C) (mean ± s.e.m.)	Graphitic C (Atomic %)	T_{IN} (°C) (mean ± s.e.m.)	Graphitic C (Atomic %)	T_{IN} (°C) (mean ± s.e.m.)	Graphitic C (Atomic %)	T_{IN} (°C) (mean ± s.e.m.)
	60.7	−27.4±0.2	61.1	−27.5±0.1	63.5	−23.8±0.2	66.1	−22.7±0.2	69.4	−21.8±0.1
13	65.3	−27.1±0.2	69.7	−25.8±0.2	67.0	−22.6±0.1	68.7	−20.2±0.2	80.1	−17.2±0.2
	68.8	−27.8±0.1	75.3	−25.2±0.2	69.7	−21.7±0.2	71.0	−18.6±0.2	83.9	−14.3±0.2
	60.7	−27.2±0.1	61.5	−27.1±0.2	63.5	−20.0±0.2	66.1	−19.3±0.1	69.4	−17.4±0.2
5.2	65.3	−27.7±0.2	69.7	−24.1±0.1	67.0	−19.3±0.3	68.7	−15.8±0.2	80.1	−13.5±0.2
	68.8	−26.9±0.2	75.3	−21.9±0.2	69.7	−18.7±0.2	71.0	−13.5±0.2	83.9	−12.4±0.2
	60.7	−27.2±0.2	61.5	−27.4±0.2	63.5	−17.9±0.2	66.1	−16.9±0.1	69.4	−15.7±0.1
0.52	65.3	−27.4±0.1	69.7	−23.2±0.2	67.0	−17.6±0.2	68.7	−14.0±0.2	80.1	−11.1±0.1
	68.8	−27.0±0.2	75.3	−20.1±0.2	69.7	−16.9±0.2	71.0	−11.7±0.2	83.9	−10.0±0.2

The volume of the water droplet is 0.2 µl; cooling rate, 5 °C min^{-1}. For each mean, the total number of measurements is about 150. Ice nucleation probability distributions (Gaussian fitting) for each mean T_{IN} are shown in Supplementary Figs. 10, 11 and 12. The content of graphitic C is obtained from the area ratio of the graphitic C sub-peak in the C 1s core-level XPS spectra (Supplementary Fig. 6). The sum of the content of graphitic and oxidative carbon is a unit, so higher content of graphitic carbon represents a lower degree of oxidation.